

Cooling of the Martian thermosphere by CO₂ radiation and gravity waves: An intercomparison study with two general circulation models

Alexander S. Medvedev,^{1,2} Francisco González-Galindo,³ Erdal Yiğit,⁴ Artem

G. Feofilov,⁵ Francois Forget,⁵ and Paul Hartogh¹

Corresponding author: A. S. Medvedev, Max Planck Institute for Solar System Research,
Justus-von-Liebig-Weg 3, 37077 Göttingen, Germany. (medvedev@mps.mpg.de)

¹Max Planck Institute for Solar System
Research, Göttingen, Germany

²Institute of Astrophysics, Georg-August
University, Göttingen, Germany

³Instituto de Astrofísica de Andalucía,
CSIC, Granada, Spain

⁴Space Weather Group, School of Physics
Astronomy and Computational Sciences,
Fairfax, VA, USA

⁵Laboratoire de Météorologie Dynamique,
CNRS, Paris, France.

Abstract. Observations show that the lower thermosphere of Mars (\sim 100–140 km) is up to 40 K colder than the current general circulation models (GCMs) can reproduce. Possible candidates for physical processes missing in the models are larger abundances of atomic oxygen facilitating stronger CO_2 radiative cooling, and thermal effects of gravity waves. Using two state-of-the-art Martian GCMs, the Laboratoire de Météorologie Dynamique and Max Planck Institute models that self-consistently cover the atmosphere from the surface to the thermosphere, these physical mechanisms are investigated. Simulations demonstrate that the CO_2 radiative cooling with a sufficiently large atomic oxygen abundance, and the gravity wave-induced cooling can alone result in up to 40 K colder temperature in the lower thermosphere. Accounting for both mechanisms produce stronger cooling at high latitudes. However, radiative cooling effects peak above the mesopause, while gravity wave cooling rates continuously increase with height. Although both mechanisms act simultaneously, these peculiarities could help to further quantify their relative contributions from future observations.

1. Introduction

The lower thermosphere of Mars (\sim 100–140 km) is the gateway between the atmosphere and space. It is affected simultaneously from below and above by various dynamical and radiative processes. Spacecraft decelerate and modify their orbits in this region by dipping into denser layers. The knowledge of processes that control the lower thermosphere, and the ability to predict its state and evolution are of great importance for planning and performing future aerobraking operations. Temperatures and densities in this region also regulate the physical processes responsible for atmospheric escape [*Valeillet et al.*, 2009; *Yagi et al.*, 2009]. A precise characterization of the lower thermosphere is thus a necessary step towards a better understanding of the long-term evolution of the Martian atmosphere.

Recent observations have shown that the lower thermosphere is systematically colder than general circulation models (GCMs) predict [*Forget et al.*, 2009; *McDunn et al.*, 2010]. This discrepancy indicates that there is a major gap in our understanding of the physics and dynamics of the lower thermosphere, which is addressed in this paper.

The most comprehensive dataset to date covering the lower thermosphere has been collected with the SPICAM (Spectroscopy for the Investigation of the Characteristics of the Atmosphere of Mars) instrument onboard the Mars Express (MEX) orbiter [*Bertaux et al.*, 2006; *Forget et al.*, 2009]. It contains vertical profiles of temperature and density at altitudes between 50 and 140 km retrieved from observations of stellar occultations in UV [*Quémerais et al.*, 2006]. A comparison with simulations using the Laboratoire de Météorologie Dynamique (LMD) Mars GCM has revealed that the observed temperatures are, generally, 10 to 40 K lower than those simulated, and that this difference

apparently increases with height [Forget *et al.*, 2009]. Further intercomparison with the MEX/SPICAM data has been performed by McDunn *et al.* [2010] using an alternative modeling framework – the Mars Thermosphere General Circulation Model (MTGCM) coupled with the NASA Ames Mars General Circulation Model (MGCM). They also found that the simulated atmosphere above the mesopause was consistently warmer, and that the model mesopause was often too low. Accelerometers onboard spacecraft during aerobraking phases are an additional, although limited, source of data on density and temperature in the lower thermosphere [Keating *et al.*, 1998; Tolson *et al.*, 2002, 2007; Withers, 2006]. These measurements have been compared with the predictions from MTGCM–MGCM [Bougher *et al.*, 2006] and LMD–MGCM [González-Galindo *et al.*, 2009b]. The two models agreed well in simulating the latitudinal cross-sections of temperature at \sim 120 km, but, again, they turned out to be approximately 35 K higher than those observed [González-Galindo *et al.*, 2010, Figure 9].

Certainly, such warm model biases require an explanation. One of the offered reasons links the errors to the uncertainties in specifying the airborne dust. Bell *et al.* [2007] have shown that simulations in the mesosphere and lower thermosphere are very sensitive to distributions of aerosol below. Adjusting the amount of the airborne particles and/or their physical properties can nudge simulations closer to observations during certain periods and locations [Forget *et al.*, 2009; McDunn *et al.*, 2010]. To estimate global effects of atmospheric dust, Medvedev *et al.* [2013] performed simulations with the Max Planck Institute (MPI) GCM using the aerosol optical depth measured by the Mars Climate Sounder onboard Mars Reconnaissance Orbiter (MCS–MRO), and by the Thermal Emission Spectrometer onboard Mars Global Surveyor (TES–MGS). They found that,

during major dust storms, temperature in the lower thermosphere drops by several tens of Kelvin degrees, which is comparable to the systematic model bias mentioned above. However, there are two major shortcomings with using only the diabatic effects of lower atmospheric dust to explain the systematically warmer mesosphere simulated by GCMS. First, the dust-induced cooling in the mesosphere and lower thermosphere (MLT) occurs only during storms. Second, not all dust storms result in a uniform cooling of the lower thermosphere. The response is more complex: polar regions during equinoctial storms, and low latitudes during solstitial events, on the contrary, experience warmings.

Clearly, key physical mechanisms are missing in current GCMs. Two candidates have emerged to date to reconcile the simulated temperatures with the observations by SPI-CAM in the lower thermosphere: the CO₂ radiative cooling, and gravity wave (GW) heating/cooling. In this paper, we analyze them with two currently available Martian GCMs, which self-consistently cover the atmosphere from the surface to the thermosphere: the LMD and MPI MGCMs. They are based on different dynamical cores, and employ largely independent suites of physical parameterizations. These differences allow us to separate the effects imposed by each mechanism from possible deficiencies of individual GCMs.

The outline of this paper is the following. Section 2 presents the scientific background and past work concerning the role of CO₂ cooling and GW heating/cooling in the atmosphere of Mars. The numerical tools (MPI, LMD GCMs, and the GW scheme) used in this study are briefly described in Section 3. The setup of the models and numerical experiments are outlined in Section 4. Results of simulations with horizontally uniform (one-dimensional) vertical profiles of atomic oxygen volume mixing ratio are described in Section 5, while effects of latitudinal variations of oxygen are analysed in Section 6.

Net heating/cooling rates and their relationship with the meridional circulation are discussed in Section 7. The simulated neutral densities are presented in Section 8, and the conclusions are drawn in Section 9.

2. Background and Past Work

Atmospheric cooling by CO_2 is created by radiative transfer in the $15\text{-}\mu\text{m}$ band. Under the breakdown of local thermodynamic equilibrium (non-LTE), collisions with atomic oxygen O facilitate energy exchange between the kinetic energy of CO_2 molecules (temperature) and their excited vibrational states. Hence, cooling rates are proportional to $[\text{O}]$ abundances and the CO_2 -O quenching rate coefficient, k_{VT} . Observations of $[\text{O}]$ in the Martian atmosphere are sparse, and those available show a substantial variability [Stewart *et al.*, 1992]. The problem is aggravated by the uncertainty of the k_{VT} , the value of which differs by a factor of 3–4 between laboratory measurements and atmospheric estimates on Earth [Feofilov *et al.*, 2012]. At the moment, both MPI and LMD models use the “median” value of $k_{VT} = 3.0 \cdot 10^{-12} \text{ cm}^3 \text{ s}^{-1}$, but the exact value is an open and important question for all CO_2 -containing planetary atmospheres. These uncertainties with the GCM input, especially in the atomic oxygen density that varies by orders of magnitude, translate into the ambiguity with cooling rates, and, ultimately, with simulated temperatures. According to this hypothesis, the overestimation of temperature in the lower thermosphere is due to the underestimation of $[\text{O}]$ abundances [Forget *et al.*, 2009]. As described in section 5, the parameterizations that simulate the CO_2 cooling in Martian GCMs have traditionally used a prescribed constant atomic oxygen profile. Forget *et al.* [2009] showed how using instead the temporally and spatially varying atomic oxygen abundance predicted by the LMD–MGCM produced significantly lower temperatures in

the lower thermosphere, which were in a better agreement with SPICAM measurements.

McDunn et al. [2010] have also illustrated with the MTGCM–MGCM framework that an increase of atomic oxygen volume mixing ratio by 50% yielded 5 to 10 K lower model temperatures.

The other mechanism pertains to cooling by internal gravity waves (GWs) that are continuously generated by a variety of meteorological processes in the lower atmosphere, such as, flow over topography, convection, storms, and front systems. GWs effectively propagate upward transporting momentum and energy, and their amplitudes exponentially grow with height, compensating for the decay of density. At higher altitudes, they become increasingly unstable, and break and/or dissipate due to an intensification of dissipative processes, such as, nonlinear interactions, molecular diffusion and thermal conduction [*Yiğit and Medvedev*, 2015, and reference therein]. Thus, gravity wave momentum deposition to the mean flow, or “gravity wave drag”, causes wind acceleration or deceleration. Mechanical energy of obliterating waves irreversibly converts into heat, and thus, affects temperature. In addition, dissipating GWs induce a downward sensible heat flux. In a freely propagating GW harmonic, oscillations of temperature (T') and vertical velocity (w') are in opposite phase, and the mean sensible heat flux associated with the harmonic $\overline{w'T'} = 0$. Dissipation introduces a phase shift between T' and w' , and $\overline{w'T'}$ is no longer zero, always negative, that is, directed downward. Vertical divergence of the wave-induced sensible heat flux, $-\rho^{-1}d(\rho\overline{w'T'})/dz$, enters the thermodynamic equation for the mean temperature, and represents the cooling/heating rate: cooling above the dissipation level, and heating below [*Medvedev and Klaassen*, 2003; *Yiğit and Medvedev*, 2009; *Medvedev and Yiğit*, 2012]. Such waves have horizontal scales from tens to hundreds

of kilometers, which, in most cases, are not resolved by GCMs. Therefore, the effects of subgrid-scale GWs in GCMs must be parameterized.

The most recent and comprehensive parameterization originally developed for and utilized in Earth GCMs extending from the lower atmosphere into the thermosphere is the spectral nonlinear GW scheme of *Yiğit et al.* [2008]. *Medvedev et al.* [2011a] have successfully applied this scheme to estimate GW effects in the Martian thermosphere. These effects were shown to be significant, and can thus not be neglected above ~ 100 km. Further interactive simulations with the *Yiğit et al.* [2008] scheme implemented into the MPI–MGCM have demonstrated that GWs dramatically change the lower thermospheric circulation. Their dynamical effects are reminiscent of those in the terrestrial MLT [*Medvedev et al.*, 2011b]. The MGCM simulations of *Medvedev and Yiğit* [2012] have also shown that GW-induced thermal effects yielded the necessary cooling rates in order to reproduce the lower thermospheric temperatures that are 10–40 K colder in observations than in previous model simulations. Therefore, their simulations closely match the SPICAM measurements analyzed in the work of *Forget et al.* [2009]. The inclusion of parameterized effects of GWs into the MPI–MGCM has allowed it to reproduce for the first time the latitudinal night-time temperature structure at ~ 120 km derived from aerobraking measurements of *Bouger et al.* [2006]. These simulations predicted, in particular, that most of the cooling takes place at high latitudes, which cannot be validated at the moment due to an insufficient coverage of the SPICAM database.

3. Numerical Tools

3.1. The Max Planck Institute General Circulation Model

This GCM is based on a spectral dynamical core, and employs physical parameterizations described in detail in the works of *Hartogh et al.* [2005, 2007], and *Medvedev and Hartogh* [2007]. The vertical domain extends from the surface to approximately 150–160 km (model top pressure $p = 3.6 \times 10^{-6}$ Pa). It is represented by 67 hybrid levels: terrain-following near the surface, and pressure-based in the middle and upper atmosphere. The simulations to be presented here have been performed at a T21 horizontal spectral truncation, which is equivalent to a 64×32 –gridpoint resolution in longitude and latitude, correspondingly.

Heating and cooling rates due to the radiative transfer in the gaseous CO₂ are calculated with separate parameterizations for LTE and non-LTE conditions. In the lower atmosphere, an LTE radiation scheme of *Nakajima et al.* [2000] based on the k -distribution method is used. In the middle and upper atmosphere, the exact non-LTE code ALI-ARMS of *Kutepov et al.* [1998]; *Gusev and Kutepov* [2003] optimized with respect to a number of vibrational levels involved in the problem and with the opacity distribution function method [*Feofilov et al.*, 2006; *Feofilov and Kutepov*, 2012] is applied for calculations in the CO₂ 15- μm band. The accuracy of the optimized model for cooling/heating rate calculations above 70 km altitude is $\approx 10\text{--}15\%$ with respect to line-by-line calculations. The profiles of heating/cooling rates from the LTE and non-LTE schemes are smoothly merged between 60 and 70 km. Heating rates due to absorption of solar radiation in the near-IR bands of CO₂ are accounted for with a simple parameterization given by formulae 1 and 2 of *González-Galindo et al.* [2009a]. Heating due to absorption of UV and EUV solar radiation by CO₂ in the upper atmosphere is calculated for 37 spectral intervals between

5 and 105 nm. The scheme uses the solar EUV flux model of *Richards et al.* [1994], and the heating efficiency 0.22 [*Fox et al.*, 1996].

The model employs the MSTRN-X radiative scheme [*Nakajima and Tanaka*, 1986] for calculations of heating and cooling rates due to absorption, scattering and emission by atmospheric dust. The scheme uses 19 representative wavelength bands: 9 in the visible and 10 in the IR spectral range. The adopted optical properties of dust particles are described in the work of *Hartogh et al.* [2005, section 3.3].

3.2. The Laboratoire de Météorologie Dynamique General Circulation Model

The LMD–MGCM solves the primitive equations using a grid-point discretization by a dynamical solver inherited from the terrestrial LMDZ GCM [*Forget et al.*, 1999]. It is a ground-to-exosphere (top at about 250 km from the surface) model. The grid used for this work includes 64×48 (in longitude and latitude) points in the horizontal, with 49 vertical hybrid levels.

The physical parameterizations included in the LMD–MGCM are described in [*Forget et al.*, 1999; *Montmessin et al.*, 2004; *Lefèvre et al.*, 2004], and for processes important in the upper atmosphere in [*Angelats i Coll et al.*, 2005; *González-Galindo et al.*, 2005, 2009a]. The latest model improvements that concern the upper atmosphere and described by *González-Galindo et al.* [2013], have also been included in the simulations presented here. In particular, the improved 15- μm cooling scheme using five CO₂ bands, a calculation of the full exchange between atmospheric layers, and the possibility of including the spatially and temporally variable atomic oxygen density as self-consistently provided by the photochemical model described in [*González-Galindo et al.*, 2009a, 2013], is used in this work. Note, however, that for the simulations included here, constant atomic oxygen profiles as

described in sections 5 and 6 are used instead. For the UV heating, the scheme described in *González-Galindo et al.* [2005] is used with a heating efficiency of 0.22, identical to that employed in the MPI–MGCM.

The LMD–MGCM includes a parameterization of effects of subgrid-scale orographic gravity waves, as described in the work of [Forget *et al.*, 1999]. Previous works [*Angelats i Coll et al.*, 2005], however, have shown that the effects of such waves in the Martian thermosphere are negligible. A parameterization for non-orographic gravity waves is not included in the current version of the model.

3.3. The Extended Gravity Wave Parameterization

This GW parameterization has been described in full detail in the work by *Yiğit et al.* [2008], and its implementation to the MPI–MGCM and setup are given in the work of *Medvedev et al.* [2011b]. The scheme solves the equation for the vertical propagation of horizontal momentum fluxes F for subgrid-scale GW harmonics, and accounts for their refraction by larger-scale wind and temperature, dissipation and breaking. For a single harmonic j of the spectrum, the equation has the form

$$\frac{dF_j}{dz} = -\left(\frac{\rho_z}{\rho} + \beta_{non}^j + \beta_{mol}^j\right)F_j, \quad (1)$$

where $F_j = \overline{u'_j w'_j}$ is the momentum flux per unit mass; u' and w' are the wave perturbations of the horizontal and vertical winds, correspondingly; the overline denotes an appropriate averaging over subgrid scales; ρ is the altitude dependent neutral mass density, where the subscript “z” denotes a derivative with respect to the altitude. The vertical damping rates β^j for a given harmonic in (1) are due to saturation/breaking associated with nonlinear effects in the individual harmonic, and/or caused by interactions with others in the spec-

trum (β_{non}^j), and due to molecular diffusion and thermal conduction (β_{mol}^j). The vertical profiles of F_j are formed by a competition between growing wave amplitude in response to the decreasing density, and the decay due to dissipation and/or breaking. The momentum flux divergence for a particular harmonic yields the momentum deposition to the mean flow, $a_j = \rho^{-1}d(\rho F_j)/dz$, and the net acceleration/deceleration consists of contributions of all a_j . Similarly, dissipating GW harmonics produce heating/cooling rates, which affect the mean temperature, that is, the energy balance of the neutrals. They can conveniently be expressed in terms of a_j [Medvedev and Klaassen, 2003, Equation 36]:

$$E^j = c_p^{-1} a_j (c_j - \bar{u}), \quad Q^j = \frac{H}{2R\rho} \frac{d}{dz} [\rho(c_j - \bar{u})], \quad (2)$$

where E^j is the irreversible heating due to conversion of the wave mechanical energy into heat, Q^j is the differential cooling/heating due to the wave-induced sensible heat flux, c_p is the specific heat at constant pressure, H is the density scale height, \bar{u} is the mean (GCM-resolved) wind, and c_j is the horizontal phase speed of the j -th harmonic. The total heating and/or cooling rate is the sum of contributions of individual harmonics. Within the framework of the GW parameterization, Equations (1) and (2) are solved interactively, and the calculated tendencies are accounted for in the momentum and thermodynamic energy equations of the GCM.

Solution of (1) requires a specification of F_j at a certain height. Since most of GWs are being generated in the lower atmosphere, we prescribed the source level at $p = 260$ Pa. The incident spectrum in the simulations was represented by 28 harmonics, whose horizontal phase speeds were distributed normally around the local wind speed. The magnitudes of the fluxes were normalized to match the observed background GW-related variances on Mars [Creasey *et al.*, 2006]. Such choice of the source spectrum is based on

the extensive experience with applications of the extended GW scheme to GCM studies on Earth [e.g., *Yiğit et al.*, 2012, 2014; *Yiğit and Medvedev*, 2009, 2012] and Mars [*Medvedev et al.*, 2011b, 2013; *Medvedev and Yiğit*, 2012], and is discussed in detail there.

4. Model and Experiment Setup

In order to exclude a possible influence from below associated with dust variability, we performed simulations for low-dust equinox period around $L_s = 0^\circ$. The aerosol was taken to be well mixed vertically, and prescribed by the *Conrath* [1975] formula:

$$q(z) = q_0 \exp \left\{ \nu \left[1 - \left(\frac{p_0}{p} \right) \right] \right\}, \quad p < p_0, \quad (3)$$

where q is the dust mixing ratio, $q_0 = q(z = 0)$, p is pressure, $p_0 = 610$ Pa is the global-mean surface pressure, and the Conrath parameter $\nu = 0.007$ corresponds to a practical absence of dust radiative effects above 60–70 km. q was normalized such that the total optical depth in visible wavelengths τ was uniformly equal to 0.2. Simulations were conducted for the solar activity close to a minimum (solar flux index $F_{10.7} = 80 \times 10^{-22}$ W m² Hz⁻¹).

In each scenario described below, the GCMs were run for at least 30 sols preceding $L_s = 0^\circ$ to exclude adjustment processes, and the outputs from 15 sols immediately following this moment were analyzed. Therefore, unless stated otherwise, the figures are based on 15-sol averaged fields.

5. Results with One-Dimensional Oxygen Profiles

The only *in situ* measurements of atomic oxygen in the Martian thermosphere have been performed with the neutral mass spectrometers during the descents of Viking 1 and 2 in the altitude range of 120 km [*Hanson et al.*, 1977]. Other constraints on atomic

oxygen abundances have been inferred from UV airglow observations [e. g., *Stewart et al.*, 1992; *Huestis et al.*, 2008]. The measurements as well as photochemical modeling have demonstrated that atomic O concentrations are highly variable, and depend on local time, geographical location, season, solar activity, etc. In this section, we explore the response of the atmosphere to gross changes of volume mixing ratios [O] represented by two horizontally uniform and temporally constant vertical profiles, which are plotted in Figure 1. The first one (shown in red) is taken from photochemical simulations of *Nair et al.* [1994]. It was routinely adopted for simulations with many Martian GCMs utilizing the non-LTE CO₂ cooling parameterization of *López-Valverde and López-Puertas* [2001] (in the so-called “static oxygen” version) [e.g., *Angelats i Coll et al.*, 2005; *Bell et al.*, 2007; *González-Galindo et al.*, 2010; *McDunn et al.*, 2010]. A very similar distribution of [O] was used in simulations with the MPI-GCM, although in conjunction with the different radiation scheme [e.g., *Hartogh et al.*, 2005; *Medvedev and Hartogh*, 2007; *Medvedev et al.*, 2011b, 2013]. The second profile (plotted with blue dashed lines, and hereafter referred to as MCD-1D) has been obtained by averaging the output from the Mars Climate Database (MCD). The latter is based on the LMD–MGCM simulations with interactive photochemistry, and provides distributions of [O] as functions of latitude, longitude, pressure level, and local time for each Martian “month”, for $L_s = 0 - 30^\circ$ in our particular case. The MCD-1D profile describes a scenario with an increased atomic oxygen abundance – the volume mixing ratio is greater than that of *Nair et al.* [1994] everywhere in the middle and upper atmosphere: by about a factor of 8 at $p = 10^{-3}$ Pa, and ~ 4 at $p = 10^{-5}$ Pa. Despite such significant differences, both profiles are well within the limits of variations that follow from photochemistry models, and from a limited number of observations.

5.1. Impact of Atomic Oxygen Variations

To compare the net effects on temperature introduced by these profiles, the first series of simulations have been performed without including the GW parameterization. The corresponding zonal mean temperatures are presented in Figure 2. In the runs with the low oxygen abundance (marked as “Nair94”), the simulated temperatures differ by not more than 15 K, except in the vicinity of the poles (Figure 2a,c). Both models simulated a relatively “warm” mesopause, and placed it between $p = 10^{-2}$ and 10^{-3} Pa. The two simulations also yield very close temperature gradients in the lower thermosphere, especially in low and middle latitudes. When the runs were repeated with the MCD-1D atomic oxygen profile (“large” O abundances), the simulated temperatures expectedly dropped in the upper portions of the domains. The differences with the “low oxygen” runs are highlighted with blue shades in Figure 2b,d. It is seen that the differences are the largest in middle and high latitudes (~ -40 K), and are around -20 K elsewhere in the lower thermosphere. Accordingly, the mesopauses in the MCD-1D simulations are about 20 K colder (120 K), and located somewhat higher (at approximately 10^{-3} Pa). There are also differences in the response of both models to the increased [O]. It is by ≈ 15 K greater above the mesopause in the MPI model, and by about same amount larger at the mesopause in the LMD–MGCM.

Further insight can be gained from analyzing the radiative heating/cooling rates, which are plotted for the MCD-1D runs in Figure 3. Both GCMs employ the same parameterization for near-IR CO_2 heating, and, therefore, the calculated mean rates are within the margins of errors due to numerics (Figure 3a,d). The maximum of heating (≈ 90 K sol^{-1}) occurs just below the mesopause, and steeply decreases above. On the contrary, the UV-

EUV heating rates continuously increase above the mesopause. This heating rate is also similar in both simulations (with a somewhat stronger heating in the LMD–MGCM) despite the completely independent parameterizations used in the two models (Figure 3c,f). Cooling rates due to the $15 \mu\text{m}$ CO_2 band differ the most. Unlike the EUV and near-IR heating rates, they strongly depend on temperature. In both models, CO_2 cooling rates increase with height in the mesosphere, have local minima at the mesopause (as a response to temperature minima), reach maxima above the mesopause, and decay with height in the lower thermosphere (Figure 3b,e). Cooling is stronger in high latitudes in both GCMs, which is a consequence of higher polar temperatures. However, CO_2 cooling rates in the LMD model are overall larger than in the MPI–GCM, especially near the poles: up to -400 K sol^{-1} poles in the LMD run versus $\sim -110 \text{ K sol}^{-1}$ in the MPI simulation. In the regions where the model temperatures are closer, the corresponding cooling rates are closer as well, for instance, around -80 K sol^{-1} at $p = 0.01 \text{ Pa}$ in low latitudes. Qualitatively, both models demonstrate a similar response to variations of atomic oxygen with larger cooling rates in the LMD model.

5.2. Impact of Gravity Waves

After exploring the model responses to enhanced CO_2 cooling due to the prescribed atomic oxygen, we turn to thermal effects of gravity waves. For that, we included the GW scheme in the MPI–GCM, and repeated the simulations. Results for the MCD-1D scenario are plotted in Figure 4. Two distinctive effects of GWs are seen in the temperature field (Figure 4a). They are (a) the colder lower thermosphere, especially in high latitudes, where the simulated temperature dropped by up to 20 K, and (b) warmer (by up to 9 K) polar regions in the middle atmosphere. In the run with the “low” atomic oxygen scenario

(not shown here), the GW-induced changes in the thermosphere were even stronger (more than 30 K colder poles in the thermosphere), but qualitatively similar. Such effects of gravity waves have previously been reported for solstice conditions [Medvedev and Yiğit, 2012], and then throughout the Martian year [Medvedev *et al.*, 2013, Figure 1].

As a response to the altered simulated temperature, CO_2 cooling rates in Figure 4b have also changed with respect to those in Figure 3b for the run without GWs. In particular, peak values increased from -80 to -120 K sol^{-1} over warmer polar regions in the mesosphere, and decreased from -100 to -60 K sol^{-1} in the colder lower thermosphere. GW-induced heating and cooling rates in Figure 4c,d can now be compared against those due to radiative transfer in CO_2 molecules. Firstly, the former takes place, generally, higher than the latter. Secondly, the magnitudes of GW heating and cooling (E^j and Q^j in Equation 2, correspondingly), are comparable or larger than those by CO_2 . Thirdly, GW heating and cooling increase with height in the lower thermosphere, whereas the radiative rates reach their maxima there, and then decay with altitude. GW cooling exceeds heating everywhere in the lower thermosphere. Thus, the net effect of GWs is $\sim -100 \text{ K sol}^{-1}$ at $p = 10^{-5} \text{ Pa}$ in low and middle latitudes, and is more than $\sim -600 \text{ K sol}^{-1}$ near the poles at these heights. The enhancement of cooling/heating rates at high-latitudes is related to the stronger GW activity in polar regions, which results from more favorable propagation conditions for GW harmonics there. Such increased activity has been found in the thermosphere of Earth at solstices and equinoxes [Yiğit *et al.*, 2009, 2012, 2014], and of Mars throughout most of the year [Medvedev *et al.*, 2013]. Note that higher temperatures in the polar regions in the mesosphere are not related to direct heating by GWs, as is seen in Figures 4c,d. They are the result of the adiabatic

heating produced by the enhanced downward branch of the meridional circulation driven dynamically by GWs.

6. Results for Two-Dimensional Atomic Oxygen Distribution

Distribution of atomic oxygen in the lower thermosphere is controlled by photochemistry and transport. During equinoxes, the two-cell circulation with downward branches over the poles creates an excess of [O] in high latitudes. In this section, we quantify the effects of latitudinal variations of atomic oxygen. For that, we again use the MCD output for $L_s = 0\text{--}30^\circ$ averaged over longitudes and local times. This scenario (referred to as MCD-2D) with the atomic oxygen varying with latitude and height is consistent with the MCD-1D, as the latter is obtained by averaging the former. As seen from the corresponding altitude-height distribution in Figure 5, there is up to 5 times more atomic oxygen in polar regions than in the low- and middle latitudes, with somewhat more over the South Pole. Because of that, there is less [O] in low- and middle-latitudes in the MCD-2D scenario than in the MCD-1D.

The simulated MCD-2D temperatures are plotted in Figure 6 with contours, while the color shades denote the differences with respect to the MCD-1D runs. In full accordance with the atomic oxygen distribution, most of the changes occurred in the polar regions of the thermosphere, with more in the Southern Hemisphere. This difference reaches up to -15 K in the LMD–MGCM simulation (Figure 6b), while it is more moderate (up to -5 K, Figure 6a) in the MPI–GCM run without GWs. In the low and middle latitudes, the simulated temperatures are subtly higher (~ 1 K) as there is less [O] there. Oxygen-induced temperature change is smaller, when runs with GWs are compared (Figure 6c). In the Southern Hemisphere it is only ~ -2 K, and even somewhat positive (~ 1 K) in

the Northern high-latitudes. However the absolute values of temperature at and above the mesopause remain lower with GWs. Clearly, their thermal effects dominate in these regions.

Overall, our simulations show that the latitudinal variations of atomic oxygen do affect the simulated temperature in the lower thermosphere, however, the changes they induce are smaller than those introduced by vertical variations. On the one hand, this is because the atomic oxygen abundances differ more between the MCD-1D and *Nair et al.* [1994] scenarios than between the MCD-1D and MCD-2D. On the other hand, latitudinal gradients of [O] and of the related adiabatic heating/cooling rates alter the meridional circulation, and the associated adiabatic heating.

7. Net Diabatic Heating/Cooling

In order to explore the interplay between the radiative and gravity wave forcings, and the global dynamics further, we plotted the net diabatic rates (with the exception of UV-EUV heating, which remains constant in all the simulations) in Figure 7. The UV-EUV heating is also shown separately in the panel c. For simplicity, we consider only one-dimensional (vertically varying) [O] scenarios of *Nair et al.* [1994] and MCD-1D. All the simulations (Figure 7a,b,d,e,f) show the net diabatic heating in low latitudes up to approximately mesopause level, which is created by the CO₂ NIR heating, and cooling in middle, and especially, high latitudes. In the mean sense (when the transience is neglected), this radiative forcing is compensated by the adiabatic cooling and heating associated with the rising and sinking branches of the meridional circulation, respectively. Thus, it is seen that the mean meridional circulation in the mesosphere consists of two cells with the upwelling in low latitudes, downwelling in high latitudes, and the poleward transport in

both hemispheres. Hence, the resulting temperature is the function of a delicate balance between the diabatic and adiabatic forcing.

The 15- μm CO_2 band is the major contributor to the diabatic cooling. It depends on temperature, and, indirectly, on the meridional circulation as well. In the LMD model, these cooling rates are, in general, larger than those in the MPI–MGCM, especially in high latitudes. For the MCD-1D (“large” oxygen) scenario, the MPI simulation shows an overall increase of the CO_2 cooling rates by up to a factor of 5 near the top (Figure 7d,e). The response of the LMD–MGCM run is less straightforward: the cooling rates became even somewhat weaker in most parts in the domain despite the greater amount of atomic oxygen (Figure 7a,b). This example demonstrates that the model response to varying $[\text{O}]$ amount is highly non-linear, and driven not merely by the local diabatic forcing, but by the dynamics as well.

Gravity wave effects add to the CO_2 cooling (Figure 7f), and the total diabatic cooling rates in the MPI–GCM run turn out to be very similar to those from the LMD–MGCM simulation without GW effects. Thus, gravity waves contribute to the complexity of interactions between the diabatic forcing and dynamics in the atmosphere. Note also that GW cooling acts against the UV-EUV heating in the upper portion of the model domain, and, thus, adds to the main cooling mechanism in the thermosphere – molecular heat conduction.

8. CO_2 Density

Having explored the influence of CO_2 and GW cooling on temperature, we now turn to the neutral density, to which CO_2 is the major contributor in the lower thermosphere.

Densities at these heights impact aerobraking operations, and, therefore, their quantification is of great interest.

The effects of atmospheric temperature on density are two-fold. On the one hand, density is inversely proportional to temperature in accordance with the equation of state. Hence, colder thermospheric air at a given model pressure level implies its higher density. On the other hand, lower temperature means the smaller density scale height, and, therefore, the lower geometrical altitude of the pressure level. Thus, the net density response to the colder simulated thermosphere is not straightforward, but represents an interplay of these two effects. The height of the pressure levels (“geopotential height”) is the prognostic field in the MGCMs, and we used it to calculate the modeled densities as functions of geometrical altitudes. Figure 8 shows the vertical profiles of mean density from the simulations with the two MGCMs at three characteristic latitudes: a) at middle-to-high latitudes (60°S), b) over the equator, and c) in the polar region (80°N). Solid lines denote the simulations without GWs, and the dashed lines (in the MPI–MGCM simulations) are for runs with the GW scheme included. Between 110 and 130 km, where aerobraking operations take place, densities in the larger-oxygen MCD-1D scenario (blue lines) are up to 20% smaller than in the corresponding “Nair94” runs (red lines) in both models. Higher, the difference increases to 100% and grows with height in the MPI–GCM, while remains almost constant with height above about 130 km in the LMD–MGCM. This is consistent with the modifications of the thermal structure induced by oxygen changes in both models, mostly focused on the mesopause for the LMD–MGCM and being more important in the lower thermosphere for the MPI–GCM (see Figure 2). Gravity wave-induced cooling provides an additional contribution to the density decrease in the MPI–GCM simulations.

At low- and middle latitudes, most of temperature changes occur at the mesosphere and higher, and the densities do not differ between simulations below ≈ 100 km (Figure 8a,b,d,e). The complex dependence of density on the atmospheric temperature is particularly seen at high latitudes (Figure 8c,f), where GWs enhance the middle atmosphere polar warming, thus altering densities at much lower altitudes. At 80° around 100 km, the density simulated with accounting for GWs is $\sim 20\%$ larger in both oxygen scenarios. Higher, the vertical behavior is consistent with that shown in panels a and b.

Finally, we compare the simulated densities with the SPICAM measurements. The latter are presented in Figure 4 of the paper by *Forget et al.* [2009] as functions of the solar longitude L_s at different heights for latitudes between 50°N and 50°S . We plotted the range of their variations near $L_s \approx 0^\circ$ with horizontal bars in Figure 8a,b,d,e. At 130 km, the SPICAM measurements are around 10^{-9} kg m $^{-3}$. At 120 km, they are scattered between 4×10^{-9} and 10^{-8} kg m $^{-3}$. At 110 km, the observed densities are between 2 and 5×10^{-8} kg m $^{-3}$. It is seen that the MPI densities are on the lower end of measurements, while those from the LMD runs are somewhat larger and reproduce nicely the SPICAM measured densities, in particular for the simulations with the MCD-1D oxygen profile. Given that the simulated densities are the averaged quantities, and the SPICAM observations have been taken at certain local times being affected by thermal tides, which are particularly strong in the thermosphere, the agreement can be considered as quite good in both cases.

9. Conclusions

We explored cooling effects caused by CO₂ radiation and gravity waves (GWs) in the Martian mesosphere and lower thermosphere using two Martian general circulation models

(GCMs), the Laboratoire de Météorologie Dynamique (LMD) and Max Planck Institute (MPI) GCMs, for equinox conditions around $L_s = 0^\circ$ and low dust and solar activity. The main inferences of our simulations are listed below.

1. Within the present day uncertainties with distributions of atomic oxygen and gravity wave sources, both CO_2 and GW cooling can compensate for 10 to 40 K warmer model temperature bias in the lower thermosphere compared to observations, and produce a colder simulated mesopause.
2. CO_2 radiation under larger atomic oxygen abundances, and GWs impose stronger cooling on the Martian lower thermosphere, and result in colder model temperatures at high latitudes, especially by GWs under a low oxygen scenario.
3. Gravity wave cooling takes place, generally, higher than that due to CO_2 radiation, and GW cooling rates increase with height into the upper thermosphere, as opposed to the CO_2 rates that peak in the lower thermosphere.
4. Because most of GW activity occurs at middle and high latitudes of the thermosphere, the cooling due to GWs dominates there. The oxygen-induced amplification of the CO_2 cooling is dominant at low latitudes.
5. In addition to cooling in the thermosphere, GWs enhance the polar warmings in the mesosphere, unlike the CO_2 radiation. This temperature increase is produced dynamically (through the adiabatic heating associated with the downward branches of the meridional circulation), rather than thermally.
6. The simulated atmospheric densities at the typical altitudes for aerobraking operations decrease in around 20% at all latitudes with the larger atomic oxygen abundances. Gravity waves activity further modifies the densities in the polar regions. The simulated

densities are in overall agreement with the SPICAM measurements, in particular when the larger atomic oxygen profile is used in the simulations.

During high solar activity, the amount of atomic oxygen in the lower thermosphere increases. Likewise, gravity waves penetrate higher into the thermosphere during the active Sun periods, albeit their effects are generally weaker than during low solar activity [*Yigit and Medvedev, 2010*]. Therefore, our conclusions may change for such conditions. What are the possible pathways for further understanding the role of CO₂ and GW cooling, and eliminating the warm model bias in the lower thermosphere? Firstly, this can be done by constraining the parameterizations. For that, measurements of atomic oxygen volume mixing ratios in the thermosphere, and of GW sources in the lower atmosphere are required. Both tasks are not trivial, and cannot be performed immediately. Secondly, more detailed temperature measurements could provide the required information. In particular, latitudinal gradients throughout the thermosphere and temperature above \sim 110 km could help to clarify the role of GWs. Such data will soon become available from the Imaging UltraViolet Spectrograph (IUVS) and Neutral Gas and Ion Mass Spectrometer (NGIMS) onboard the operating MAVEN (Mars Atmosphere and Volatile EvolutioN) orbiter.

Acknowledgments. Mars Climate Database is available at <http://www-mars.lmd.jussieu.fr/mars/access.html>. Data supporting the figures are available upon request from ASM (medvedev@mps.mpg.de) and FGG (ggalindo@iaa.es).

The work was partially supported by German Science Foundation (DFG) grant ME2752/3-1. FGG was funded by a CSIC JAE-Doc contract cofinanced by the European Social Fund. FGG thanks the Spanish MICINN for funding support through the

CONSOLIDER program ASTROMOL CSD2009-00038, and through project AYA2011-23552/ESP. EY was partially supported by NASA grant NNX13AO36G.

References

Angelats i Coll, M., F. Forget, M. A. López-Valverde, and F. González-Galindo (2005), The first Mars thermospheric general circulation model: The Martian atmosphere from the ground to 240 km, *Geophys. Res. Lett.*, *32*, L04201, doi:10.1029/2004GL021368.

Bell, J. M., S. W. Bougher, and J. R. Murphy (2007), Vertical dust mixing and the interannual variations in the Mars thermosphere, *J. Geophys. Res.*, *112*, E12002, doi:10.1029/2006JE002856.

Bertaux, J.-L., et al. (2006), SPICAM on Mars Express: Observing modes and overview of UV spectrometer data and scientific results, *J. Geophys. Res.*, *111*, E10S90, doi:10.1029/2006JE002690.

Bougher, S. W., T. M. McDunn, K. A. Zoldak, and J. M. Forbes (2009), Solar cycle variability of Mars dayside exospheric temperatures: MTGCM evaluation of underlying thermal balances, *Geophys. Res. Lett.*, *36*, doi:10.1029/2008GL036376.

Bougher, S. W., J. M. Bell, J. R. Murphy, M. A. Lopez-Valverde, and P. G. Withers (2006), Polar warming in the Mars thermosphere: Seasonal variations owing to changing insolation and dust distributions, *Geophys. Res. Lett.*, *33*, L02203, doi:10.1029/2005GL024059.

Creasey, J. E., J. M. Forbes, and D. P. Hinson (2006), Global and seasonal distribution of gravity wave activity in Mars' lower atmosphere derived from MGS radio occultation data, *Geophys. Res. Lett.*, *33*, L01803, doi:10.1029/2005GL024037.

Conrath, B. J., (1975), Thermal structure of the Martian atmosphere during the dissipation of the dust storm of 1971, *Icarus*, *24*, 36–46.

Feofilov, A. G., A. A. Kutepov, A. S. Medvedev, and P. Hartogh (2012), New technique for calculating the non-LTE infrared radiative cooling/heating rates in the Martian GCM, Second workshop on Mars atmosphere modelling and observations, 27.02-03.03, 2006 Granada, Spain, Edited by F. Forget, M. A. Lopez-Valverde, M. C. Desjean, J. P. Huot, F. Lefevre, S. Lebonnois, S. R. Lewis, E. Millour, P. L. Read and R. J. Wilson. *Publisher: LMD, IAA, AOPP, CNES, ESA*, 614–617.

Feofilov, A. G., A. A. Kutepov, C.-Y. She, A. K. Smith, W. D. Pesnell, and R. A. Goldberg (2012), CO₂(ν_2)-O quenching rate coefficient derived from coincidental SABER/TIMED and Fort Collins lidar observations of the mesosphere and lower thermosphere, *Atmos. Chem. Phys.*, *12*, 9013–9023.

Feofilov, A. G. and A. A. Kutepov (2012), Infrared radiation in the mesosphere and lower thermosphere: energetic effects and remote sensing, *Surv. Geophys.*, doi:10.1007/s10712-012-9204-0.

Forget, F., F. Montmessin, J.-L. Bertaux, F. González-Galindo, S. Lebonnois, E. Quémérais, A. Reberac, E. Dimarellis, and M. A. López-Valverde (2009), Density and temperatures of the upper Martian atmosphere measured by stellar occultations with Mars Express SPICAM. *J. Geophys. Res.*, *114*, E01004, doi:10.1029/2008JE003086.

Forget, F., F. Hourdin, R. Fournier, C. Hourdin, O. Talagrand, M. Collins, S. R. Lewis, P. L. Read, J.-P. Huot (1999), Improved general circulation models of the Martian atmosphere from the surface to above 80 km, *J. Geophys. Res.*, *104*, 24155–24175.

Fox, J. L., P. Zhou, and S. W. Bougher (1996), The Martian thermosphere/ionosphere at high and low solar activities, *Adv. Space Res.*, 17, 203–218.

González-Galindo, F., J.-Y. Chaupray, M. A. López-Valverde, G. Gilli, F. Forget, F. Leblanc, R. Modolo, S. Hess, and M. Yagi (2013), Three-dimensional Martian ionosphere model: I. The photochemical ionosphere below 180 km, *J. Geophys. Res.*, 118, 2105–2123, doi:10.1002/jgre.20150.

González-Galindo, F., S. W. Bougher, M. A. López-Valverde, F. Forget, and J. Murphy (2010), Thermal and wind structure of the Martian thermosphere as given by two general circulation models, *Planet. Space Sci.*, 58, 1832–1840.

González-Galindo, F., F. Forget, M. A. López-Valverde, M. Angelats i Colli, and E. Mil-lour (2009a), A ground-to-exosphere Martian general circulation model: 1. Seasonal, diurnal, and solar cycle variation of thermospheric temperatures, *J. Geophys. Res.*, 114, E04001, doi:10.1029/2008JE003246.

González-Galindo, F., F. Forget, M. A. López-Valverde, and M. Angelats i Colli (2009b), A ground-to-exosphere Martian general circulation model: 2. Atmosphere during solstice conditions - Thermospheric polar warming, *J. Geophys. Res.*, 114, E08004, doi:10.1029/2008JE003277.

González-Galindo, F., M. A. López-Valverde, M. Angelats i Coll, and F. Forget (2005), Extension of a Martian general circulation model to thermospheric altitudes: UV heating and photochemical models, *J. Geophys. Res.*, 110, E09008, doi:10.1029/2004JE002312.

Gusev, O. A., and A. A. Kuteпов (2003), Non-LTE gas in planetary atmospheres, in *Stellar Atmosphere Modeling*, edited by I. Hubeny, D. Mihalas, and K. Werner, *ASP Conference Series*, 288, 318–330.

Hanson, W. B., S. Santanini, and D. R. Zuccaro (1977), The Martian ionosphere as observed by Viking retarding potential analyzers, *J. Geophys. Res.*, *82*, 4351–4363.

Hartogh, P., A. S. Medvedev, and C. Jarchow (2007), Middle atmosphere polar warmings on Mars: simulations and study on the validation with sub-millimeter observations, *Planet. Space Sci.*, *55*, 1103–1112.

Hartogh, P., A. S. Medvedev, T. Kuroda, R. Saito, G. Villanueva, A. G. Feofilov, A. A. Kutelev, and U. Berger (2005), Description and climatology of a new general circulation model of the Martian atmosphere, *J. Geophys. Res.*, *110*, E11008, doi:10.1029/2005JE002498.

Huestis, D. L., S. W. Bougher, J. L. Fox, M. Galand, R. E. Johnson, J. I. Moses, and J. C. Pickering (2008), Cross sections and reaction rates for comparative planetary aeronomy, *Space Sci. Rev.*, *139*, 63–105.

Keating, G. M., et al. (1998), The structure of the upper atmosphere of Mars: In-situ accelerometer measurements from Mars Global Surveyor, *Science*, *279*, 1672–1676.

Kutepov, A. A., O. A. Gusev, and V. P. Ogibalov (1998), Solution of the non-LTE problem for molecular gas in planetary atmospheres: Superiority of accelerated lambda iteration, *J. Quant. Spectrosc. Radiat. Transf.*, *60*, 199–220.

Lefèvre, S., S. Lebonnois, F. Montmessin, and F. Forget (2004), Three dimensional modeling of ozone on Mars, *J. Geophys. Res.*, *109*, E07004, doi:10.1029/2004JE002268.

López-Valverde, M. A., and M. López-Puertas (2001), Atmospheric non-LTE effects and their parameterization for Mars, ESA, Technical Report.

McDunn, T. L., S. W. Bougher, J. Murphy, M. D. Smith, F. Forget, J.-L. Bertaux, and F. Montmessin (2010), Simulating the density and thermal structure of the middle

atmosphere (≥ 80 –130 km) of Mars using the MGCM-MTGCM: a comparison with MEX/SPICAM observations, *Icarus*, 206, 5–17.

Medvedev, A. S., and E. Yiğit (2012), Thermal effects of internal gravity waves in the Martian thermosphere, *Geophys. Res. Lett.*, 39, L05201, doi:10.1029/2012GL050852.

Medvedev, A. S., E. Yiğit, T. Kuroda, and P. Hartogh (2013), General circulation modeling of the Martian upper atmosphere during global dust storms, *J. Geophys. Res.*, 118, 2234–2246, doi:10.1002/2013JE004429.

Medvedev, A. S., E. Yiğit, and P. Hartogh (2011a), Estimates of gravity wave drag on Mars: Indication of a possible lower thermospheric wind reversal, *Icarus*, 211, doi:10.1016/j.icarus2010.10.013, 909–912.

Medvedev, A. S., E. Yiğit, P. Hartogh, and E. Becker (2011b), Influence of gravity waves on the Martian atmosphere: general circulation modeling, *J. Geophys. Res.*, 116, E10004, doi:10.1029/2011JE003848.

Medvedev, A. S., and P. Hartogh (2007), Winter polar warmings and the meridional transport on Mars simulated with a general circulation model, *Icarus*, 186, 97–110.

Medvedev, A. S., and G. P. Klaassen (2003), Thermal effects of saturating gravity waves in the atmosphere, *J. Geophys. Res.*, 108, 4040, doi:10.1029/2002JD002504.

Montmessin, F., F. Forget, P. Rannou, M. Cabane, and R. M. Haberle (2004), Origin and role of water ice clouds in the Martian water cycle as inferred from a general circulation model, *J. Geophys. Res.*, 109, E10004, doi:10.1029/2004JE002284.

Nair, H., M. Allen, A. D. Anbar, Y. L. Yung, and R. T. Clancy (1994), A photochemical model of the martian atmosphere, *Icarus*, 111, 124–150.

Nakajima, T., M. Tsukamoto, Y. Tsushima, A. Numaguti, and T. Kimura (2000), Modeling of the radiative processes in an atmospheric general circulation model, *Applied Optics*, 39(N27), 4869–4878.

Nakajima, T., and M. Tanaka (1986), Matrix formulations for the transfer of solar radiation in a plane-parallel scattering atmosphere, *J. Quant. Spectrosc. Radiat. Transfer*, 35, 13–21.

Quémerais, E., J.-L. Bertaux, O. Koralev, E. Dimarellis, C. Cot, B. R. Sandel, and D. Fussen (2006), Stellar occultations observed by SPICAM on Mars Express, *J. Geophys. Res.*, 111, E09S04, doi:10.1029/2005JE002604.

Richards, P. G., J. A. Fennely, and D. G. Torr (1994), EUVAC: A solar EUV flux model for aeronomic calculations, *J. Geophys. Res.*, 99, 8981–8992.

Stewart, A. I. F., M. J. Alexander, R. R. Meier, L. J. Paxton, S. W. Bougher, and C. G. Fesen (1992), Atomic oxygen in the Martian thermosphere, *J. Geophys. Res.*, 97(A1), 91–102.

Tolson, R. H., G. M. Keating, B. E. George, P. E. Escalera, M. R. Werner, A. M. Dwyer, and J. L. Hanna (2002), Application of accelerometer data to Mars Odyssey aerobraking and atmospheric modeling, *J. Spacecraft Rockets*, 42, 435–443.

Tolson, R., G. Keating, R. W. Zurek, S. W. Bougher, C. J. Justus, D. C. Fritts (2007), Application of accelerometer data to atmospheric modeling during Mars aerobraking operations, *J. Spacecraft Rockets*, 44, 1172–1179.

Valeille, A., V. Tenishev, S.W. Bougher, M.R. Combi, and A. Nagy (2009), Three-dimensional study of Mars upper thermosphere/ionosphere and hot oxygen coronae: 1. General description and results at equinox for low solar conditions, *J. Geophys. Res.*,

114, E11005, doi:10.1029/2009JE003388.

Withers, P., and R. Pratt (2013), An observational study of the response of the upper atmosphere of Mars to lower atmospheric dust storms, *Icarus*, 225, 378–389.

Withers, P.G. (2006), MGS and Mars Odyssey accelerometer observations of the martian upper atmosphere during aerobraking, *Geophys. Res. Lett.*, 33, L02201, doi:10.1029/2005GL024447.

Yagi, M., F. Leblanc, J. Y. Chaufray, F. Gonzalez-Galindo, S. Hess, and R. Modolo (2012), Mars exospheric thermal and non-thermal components: Seasonal and local variations, *Icarus*, 221, 682–693, doi:10.1016/j.icarus.2012.07.022.

Yiğit, E., and A. S. Medvedev (2009), Heating and cooling of the thermosphere by internal gravity waves, *Geophys. Res. Lett.*, 36, L14807, doi:10.1029/2009GL038507.

Yiğit, E., and A. S. Medvedev (2010), Internal gravity waves in the thermosphere during low and high solar activity: Simulation study, *J. Geophys. Res.*, 115, A00G02, doi:10.1029/2009JA015106.

Yiğit, E., and A. S. Medvedev (2012), Gravity waves in the thermosphere during a sudden stratospheric warming, *Geophys. Res. Lett.*, 39, L21101, doi:10.1029/2012GL053812.

Yiğit, E., and A. S. Medvedev (2015), Internal wave coupling processes in Earth's atmosphere, *Adv. Space Res.*, 55, 983–1003, doi:10.1016/j.asr.2014.11.020.

Yiğit, E., A. D. Aylward, and A. S. Medvedev (2008), Parameterization of the effects of vertically propagating gravity waves for thermosphere general circulation models: Sensitivity study, *J. Geophys. Res.*, 113, D19106, doi:10.1029/2008JD010135.

Yiğit, E., A. S. Medvedev, A. D. Aylward, P. Hartogh, and M. J. Harris (2009), Modeling the effects of gravity wave momentum deposition on the general circulation above the

turbopause, *J. Geophys. Res.*, 114, D07101, doi:10.1029/2008JD011132.

Yiğit, E., A. S. Medvedev, A. D. Aylward, A. J. Ridley, M. J. Harris, M. B. Moldwin, and P. Hartogh (2012), Dynamical effects of internal gravity waves in the equinoctial thermosphere, *J. Atmos. Sol.-Terr. Phys.*, 90–91, 104–116, doi:10.1016/j.jastp.2011.11.014.

Yiğit, E., A. S. Medvedev, S. L. England, and T. J. Immel (2014), Simulated variability of the high-latitude thermosphere induced by small-scale gravity waves during a sudden stratospheric warming, *J. Geophys. Res. Space Physics*, 119, doi: 10.1002/2013JA019283.

Table 1. Approximate Height Versus Pressure

Pressure, Pa	100	10	1	0.1	0.01	0.001	0.0001	10^{-5}
Height, km	18.3	38.0	57.5	75.2	98.6	108.0	124.1	141.2

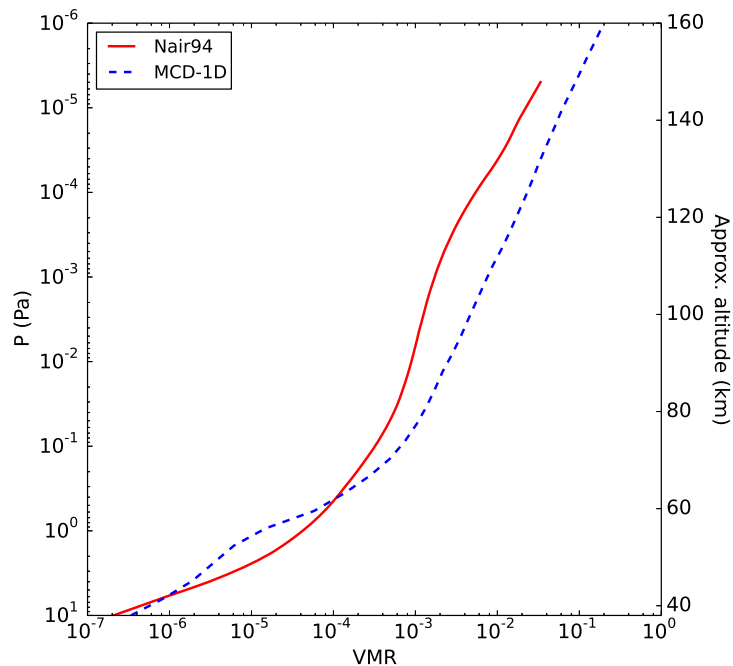


Figure 1. Profiles of atomic oxygen volume mixing ratios (in ppm) for the “low O” [Nair *et al.*, 1994] (red solid line), and “enhanced O” MCD-1D (blue dashed line) scenarios. Geometric heights of pressure levels are highly variable, but an approximate (spatially and temporally averaged) correspondence between them is plotted here, and given in Table 1. (1 Pa = 10 microbar).

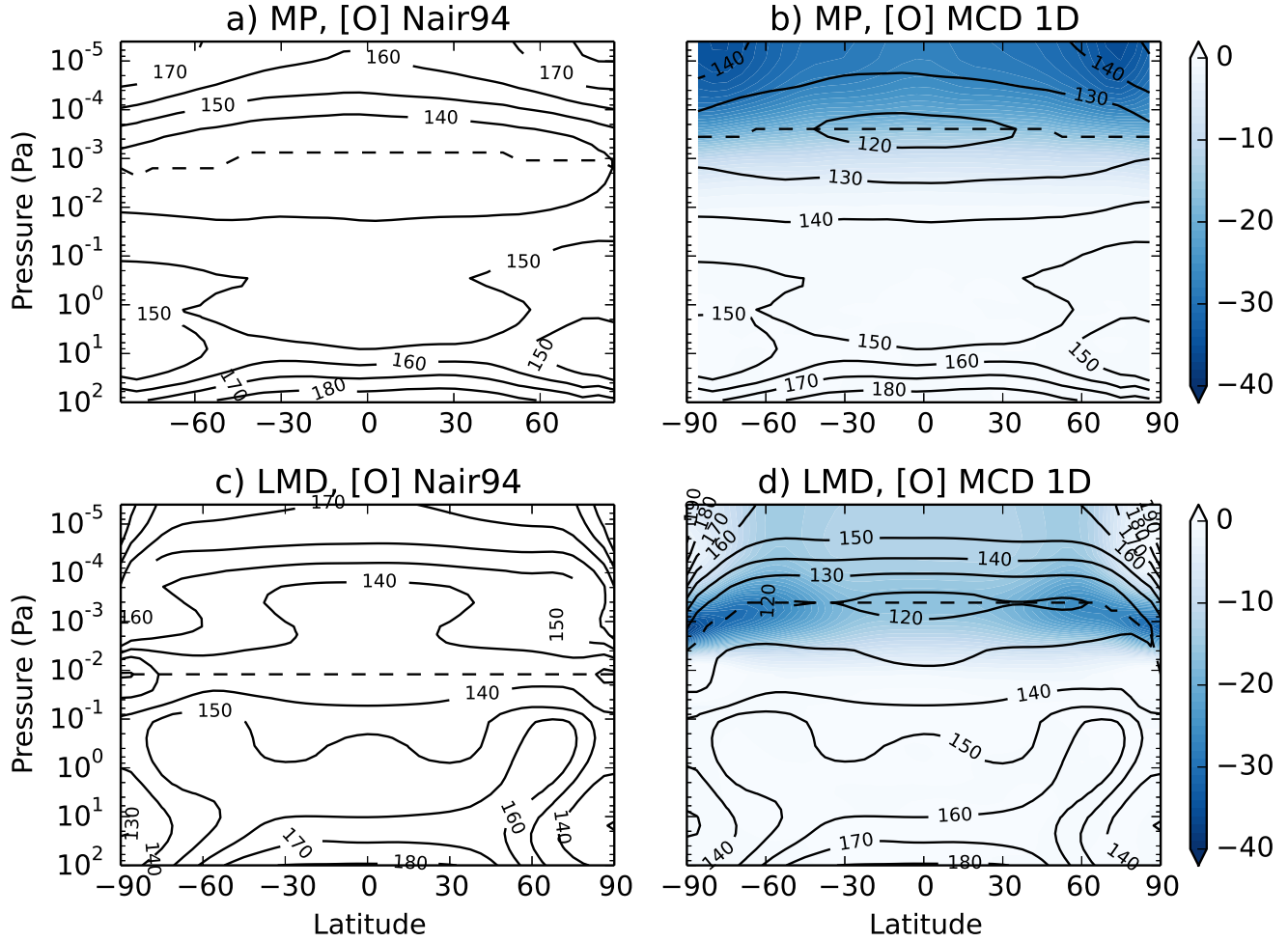


Figure 2. Zonal-mean temperature (contours) simulated without inclusion of gravity wave effects by the MPI-GCM (upper row) and LMD-MGCM (lower row). Results for the “low” oxygen [Nair et al., 1994] scenario are shown in the left column, and for the MCD-1D run are in the right column. Color shading denotes the temperature difference between the latter and the former scenarios. Black dashed line indicates the mesopause.

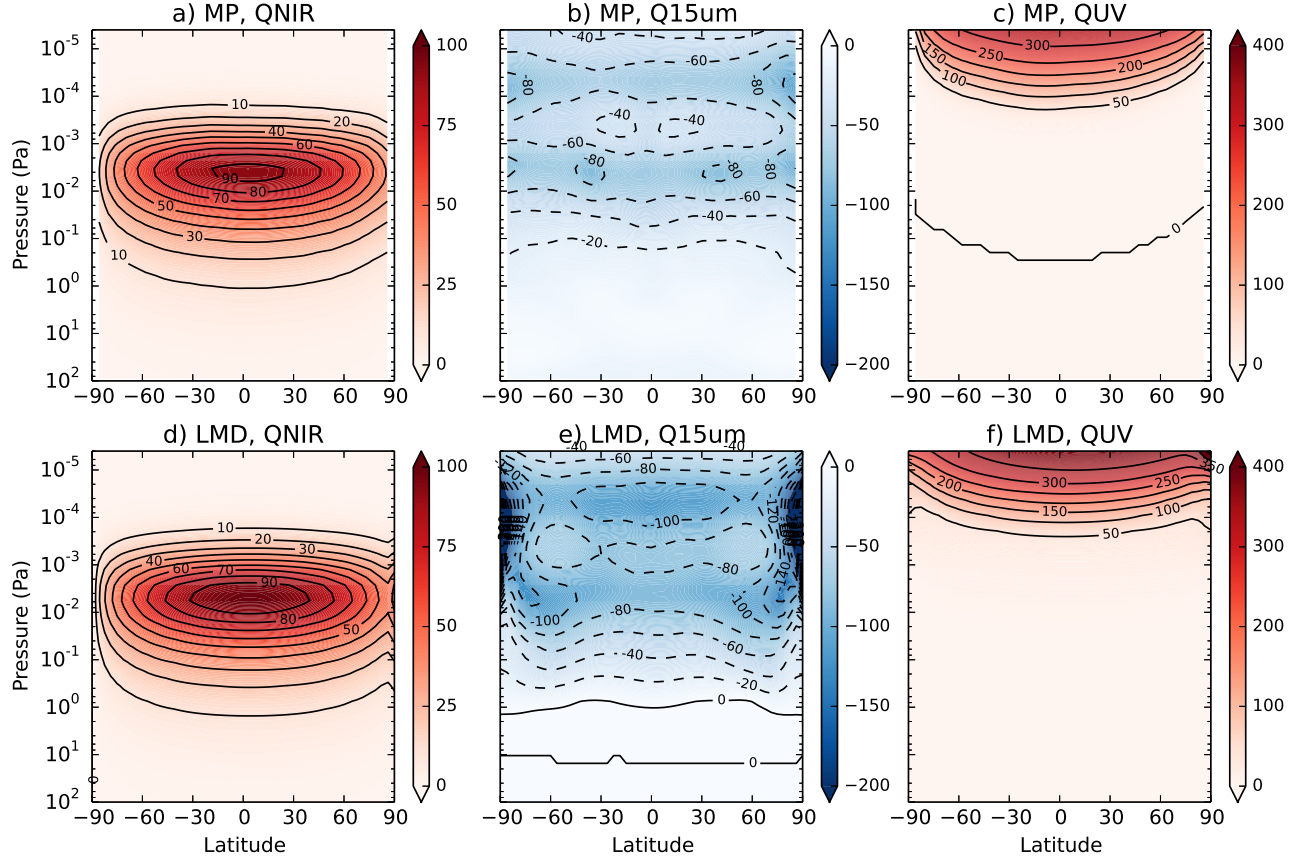


Figure 3. Radiative heating/cooling rates (in K sol^{-1}) from the runs with the MCD-1D oxygen profile without including gravity wave effects: for MPI-GCM (upper row), and LMD-MGCM (lower row). The left column is due to the near-IR CO_2 heating, the center column is due the $15 \mu\text{m}$ band CO_2 cooling, and the right column is for the UV-EUV heating.

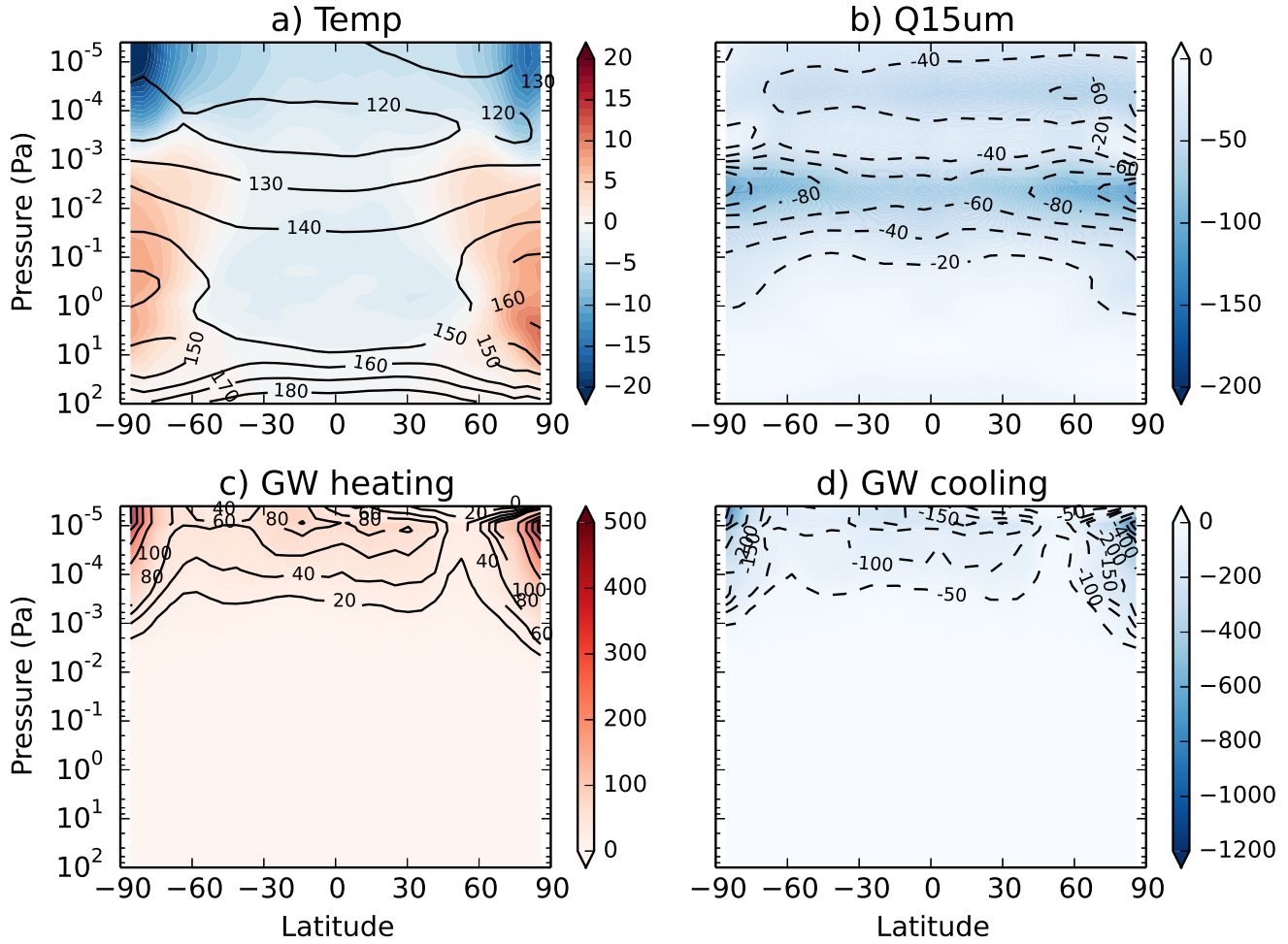


Figure 4. Results of simulations with MPI-GCM for the MCD-1D oxygen scenario. (a) Temperature (contours) and temperature difference with the MCD-1D run without the parameterized gravity wave effects (shaded). (b) 15 μm CO₂ cooling rates (contours and shaded). (c) GW-induced heating, and (d) cooling rates.

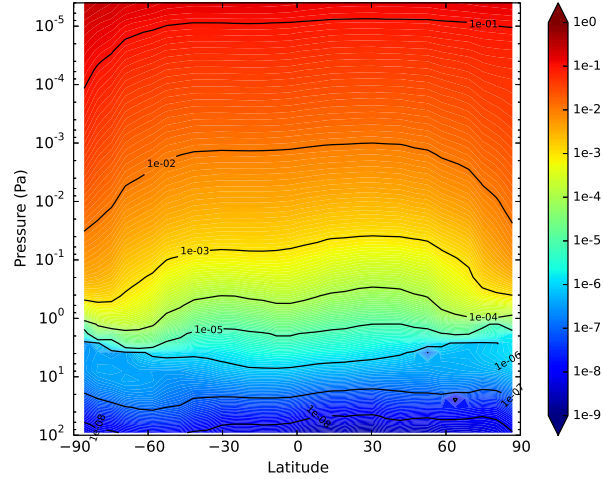


Figure 5. Latitude-height distribution of atomic oxygen volume mixing ratios for the MCD-2D scenario.

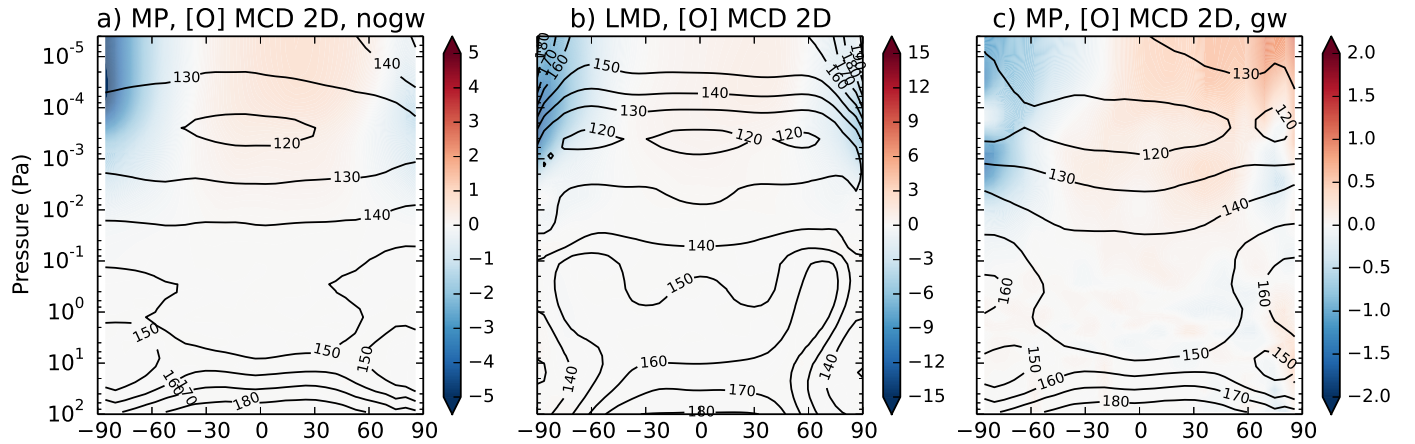


Figure 6. Temperature simulated for the MCD-2D scenario (contour lines): (a) by the MPI–MGCM without parameterized GW effects; (b) by the LMD–MGCM without GW effects; (c) by the MPI–GCM with GW parameterization included. Color shades denote temperature differences with the corresponding runs for the MCD-1D scenario.

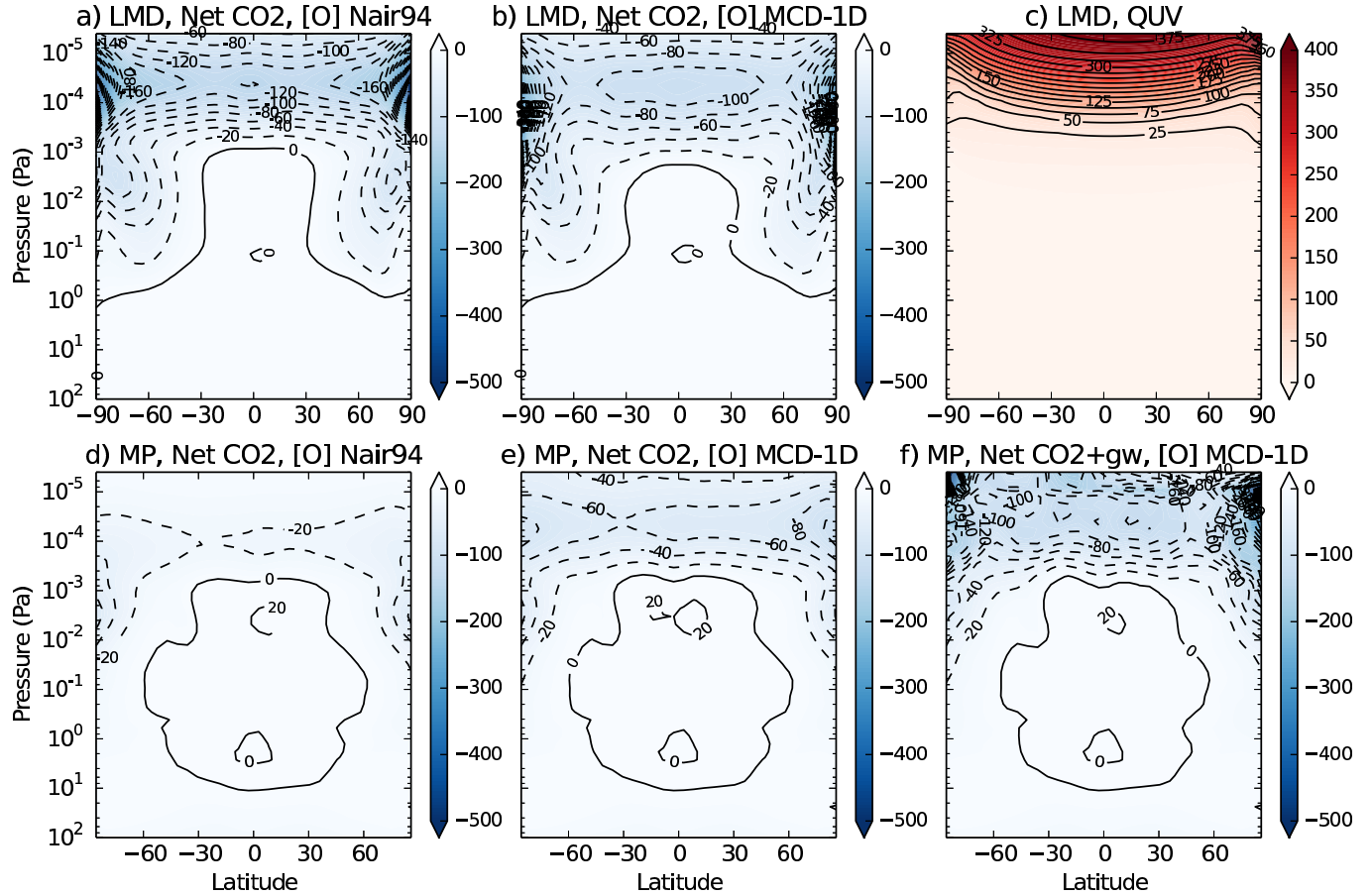


Figure 7. Net heating/cooling rates for the scenario with one-dimensional atomic oxygen profiles. Upper row is from the LMD-MGCM simulations, and the lower row is from the MPI-GCM. a) Net CO₂ radiative rates (15 μ m cooling and NIR heating) for the *Nair et al.* [1994] scenario; b) same as (a), but for the MCD-1D scenario; c) UV-EUV heating; d) same as (a), but for the MPI-GCM; e) same as in (b), but for the MPI-GCM; f) total of CO₂ radiative and gravity wave heating and cooling rates.

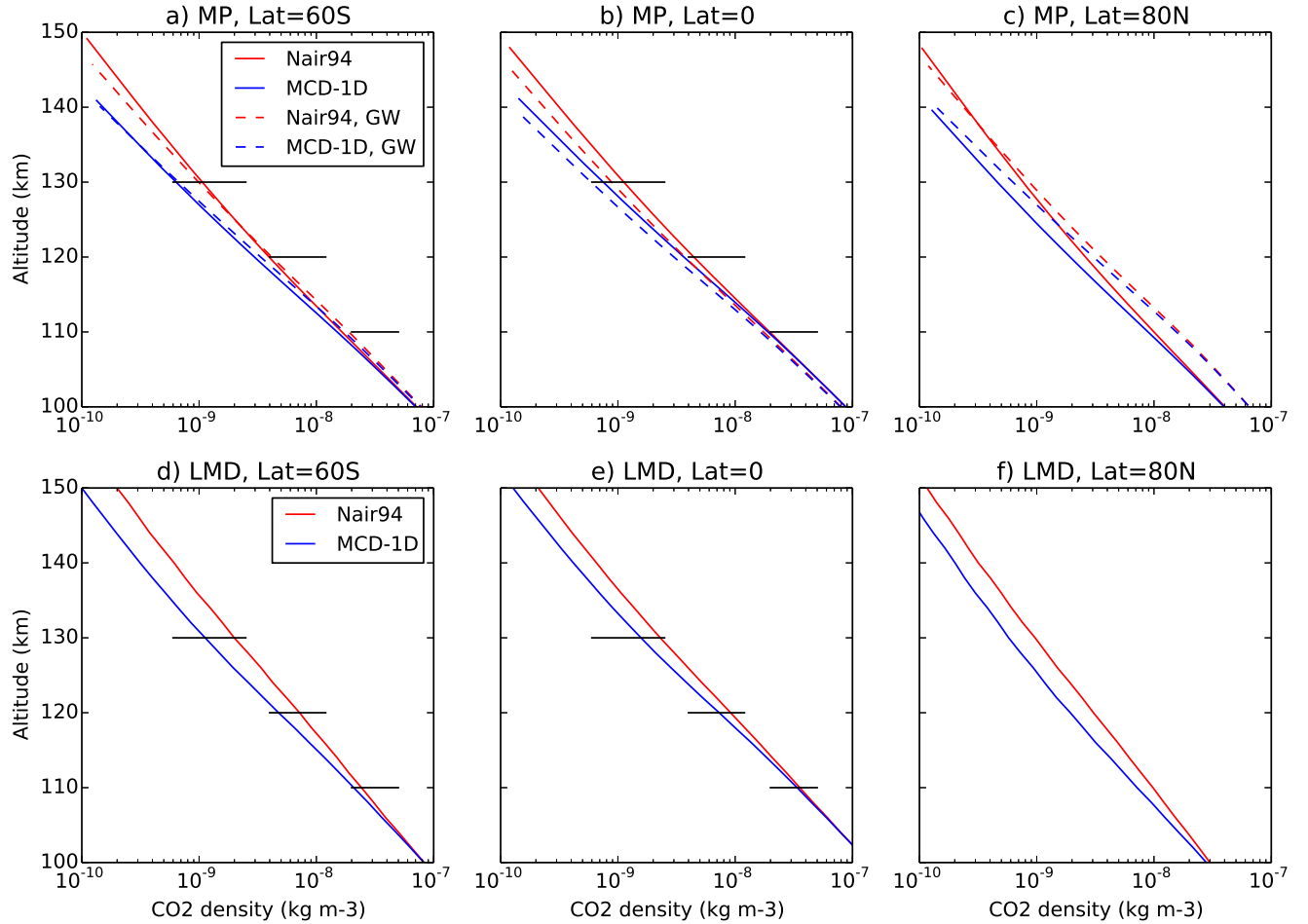


Figure 8. Mean neutral (CO_2) density simulated with the MPI–MGCM (upper row) and the LMD–MGCM (lower row) at 60°S (left column), over the equator (central column), and at 80°N (right column). Red lines correspond to the “Nair94” atomic oxygen scenario, blue lines are for the MCD-1D scenario. Solid and dashed lines denote simulations without and with GW parameterization included, respectively. Black horizontal lines represent the range of density variability from the SPICAM observations.